Science of the Total Environment 842 (2022) 156860

Contents lists available at ScienceDirect

Science of the Total Environment

journal homepage: www.elsevier.com/locate/scitotenv

Response of dryland vegetation under extreme wet events with satellite measures of greenness and fluorescence

Song Leng [a], Alfredo Huete [a,*], Jamie Cleverly [b], Xiaoliang Lu [c], Xuanlong Ma [d], Sicong Gao [e], Qiang Yu [a,c]

[a] School of Life Science, University of Technology Sydney, Ultimo, NSW, Australia
[b] College of Science and Engineering, James Cook University, Townsville, QLD, Australia
[c] State Key Laboratory of Soil Erosion and Dryland Farming on the Loess Plateau, Northwest A&F University, Yangling, Shanxi, China
[d] College of Earth and Environmental Sciences, Lanzhou University, Lanzhou, Gansu, China
[e] Land and Water, Commonwealth Scientific and Industrial Research Organisation, Adelaide, SA, Australia

HIGHLIGHTS

- The dynamics of dryland vegetation under two extreme wet events in 2010–2011 and 2016–2017 were investigated.
- SIF and EVI showed a strong correlation, and they substantially responded to the extreme wet pulses.
- C3-dominated Mulga woodland was more responsive than C4-dominated Hummock grassland.
- Satellite-based observations can more accurately estimate the productivity of dryland vegetation in wet years.

GRAPHICAL ABSTRACT

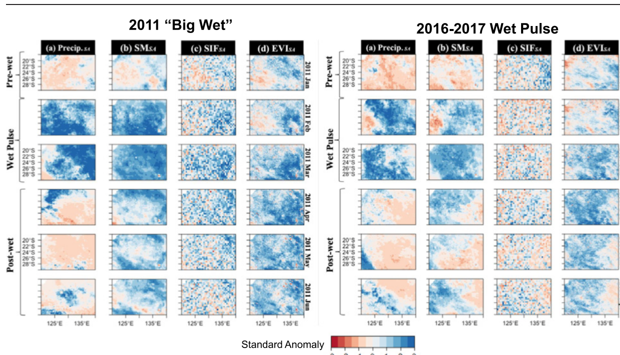

ARTICLE INFO

Editor: Manuel Esteban Lucas-Borja

Keywords:
Wet pulse
EVI
SIF
Mulga woodland
Hummock grassland

ABSTRACT

Extreme wet events in central Australia triggered large vegetation responses that contributed greatly to large global land carbon sink anomalies. There remain significant uncertainties on the extent to which these events over dryland vegetation can be monitored and assessed with satellite data. In this study, we investigated the vegetation responses of the major Australian semiarid biomes to two extreme wet events utilizing multi-satellite observations of (1) solar-induced chlorophyll fluorescence (SIF), as a proxy for photosynthetic activity and (2) the enhanced vegetation index (EVI), as a measure of canopy chlorophyll or greenness. We related these satellite observations with gross primary productivity (GPP) estimated from eddy covariance tower sites, as a performance benchmark.

The C_3-dominated Mulga woodland was the most responsive biome to both wet pulses and exhibited the highest sensitivity to soil moisture. The C_4-dominated Hummock grassland was more responsive to the 2011 “big wet” event, relative to the later 2016–2017 wet pulse. EVI swiftly responded to the extreme wet events and showed markedly amplified seasonal amplitude, however, there was a time lag as compared with SIF during the post-wet period, presumably due to the relatively slower chlorophyll degradation in contrast with declines in photosynthetic activity. Despite a robust linear SIF-GPP relationship (r^2 ranging from 0.59 to 0.85), the spatially coarse SIF derived from the Global Ozone Monitoring Experiment-2 (GOME-2) yielded high retrieval noise over the xeric biomes, hindering its capacity to capture thoroughly the dryland vegetation dynamics in central Australia. Our study highlights that synchronous satellite observations of greenness and fluorescence can potentially offer an improved understanding of dryland vegetation dynamics and can advance our ability to detect ecosystem alterations under future changing climates.

* Corresponding author.
E-mail address: alfredo.huete@uts.edu.au (A. Huete).

http://dx.doi.org/10.1016/j.scitotenv.2022.156860
Received 13 March 2022; Received in revised form 16 June 2022; Accepted 17 June 2022
Available online 21 June 2022

1. Introduction

Drylands (arid, semiarid, and subhumid), covering approximately 41 % of global land surface (Reynolds et al., 2007), play a critical role in regulating the climate system and predominantly drive the trend and variability of the land CO_2 sink (Ahlström et al., 2015; Haverd et al., 2016; Poulter et al., 2014). Studies report a massive global land carbon sink anomaly in 2010–2011 was driven by unusual growth in semiarid vegetation in the southern hemisphere, with almost 60 % of the anomaly occurring in Australia as a consequence of the record-breaking rains (Detmers et al., 2015; Ma et al., 2016; Rammig and Mahecha, 2015). Prolonged droughts and severe wet events are projected to increase in both frequency and intensity (Huang et al., 2016; Min et al., 2011) which will exacerbate impacts on water resources, ecosystems, economy, and society (Evans et al., 2017). Therefore, it is essential to enhance our understanding of dryland ecosystem functioning under future changing climate.

Australia is the driest inhabited continent worldwide, of which 70 % are encompassed with arid or semiarid ecosystems across the vast interior and dominated by three major biomes along a woodland-savanna-grassland continuum (Bowman et al., 2008; Cleverly et al., 2013a, 2013b; Cleverly et al., 2016a, 2016b; Xie et al., 2016). Among them, Hummock grasslands (Triodia spp.), Mulga woodlands (*Acacia aneura*), and Mulga shrublands varying in photosynthetic pathways (C_4 grass, C_3 tree, and C_3 shrub respectively), are widely distributed and juxtaposed in the xeric zone of central Australia (Cleverly et al., 2016a; Eamus et al., 2013). Relative to mesic vegetation, these semiarid biomes in the interior of Australia show the largest temporal variability in phenology and exhibit much greater overall responsiveness to hydro-climatic variability (Ma et al., 2013).

Quantifying the response of vegetation to extreme hydro-climatic events is crucial for effectively managing the environment and global change research (Broich et al., 2018), with observation-based methods, such as field measurement, airborne and spaceborne observation most often utilized (Yang et al., 2018). Measurements of eddy covariance data of CO_2 landscape fluxes, Eamus et al. (2016) demonstrated that Mulga woodland vegetation contributed markedly to the large 2011 anomaly in terrestrial carbon uptake. In the subsequent drought from 2011 to 2012, the massive net carbon uptake over central Australia was promptly diminished (Ma et al., 2016), of which the *Corymbia* savanna dominated by Hummock grass understory was a very large net carbon source in contrast to the extreme drought tolerance of Mulga which was approximately carbon neutral (Cleverly et al., 2016c).

Satellite remote sensing offers an approach for monitoring vegetation growth at regional, continental, or global scale (Huete et al., 2008), which is especially valuable for remote areas over most inland Australia with very sparse monitoring sites. Through normalized difference vegetation index (NDVI) as a vegetation productivity proxy derived from satellite time series data, Ratzmann et al. (2016) investigated the functional response of dryland vegetation to altered rainfall patterns over semiarid regions in Africa and indicated that higher interannual rainfall variability might force a more dynamic vegetation response. Likewise, Broich et al. (2018) found substantial differences in timing, magnitude and duration of vegetation responses and its dependence on rainfall and flooding during a period of extreme hydro-climatic variability over semiarid areas across Australia's Murray Darling Basin. Dramatic impacts of climate extremes on vegetation dynamics (as measured by EVI) with abrupt changes in phenology and productivity over southeast Australia also demonstrates that semiarid ecosystems exhibit the largest sensitivity to hydro-climatic variations (Ma et al., 2015).

In contrast to traditional vegetation indices, satellite retrievals of SIF based on energy reemitted by plants rather than reflected present a fresh manner to observe vegetation growth and response (Frankenberg et al., 2011; Guan et al., 2015; Sun et al., 2017). SIF appears to better capture interannual and seasonal variations in GPP across dryland ecosystems of southwestern North America, however SIF also exhibits limitations for estimating GPP over low productivity areas that have significant portions of bare soil (Smith et al., 2018; Wang et al., 2022). SIF can more accurately estimate GPP and further contribute to an enhanced understanding of the role of drylands in driving interannual variability of the global carbon cycle (Biederman et al., 2017). Moreover, previous studies reveal that spaceborne SIF has excellent potential to early detect drought-related and heat stress conditions across a variety of ecosystems, such as cropland, grassland, and forest (Song et al., 2018; Sun et al., 2015; Yang et al., 2018; Yoshida et al., 2015). Nevertheless, considering spatially coarse satellite-based SIF products, studies with reference to the application of SIF over heterogeneous dryland or savanna under extreme wet events thus far remain unexplored.

Numerous studies have shown that vegetation phenology and productivity in arid ecosystems are largely controlled by soil water content (Cleverly et al., 2016b; Madani et al., 2017), accordingly it can be used as an excellent predictor for plants growth under changing climates. Chen et al. (2014b) illustrated that a strong positive correlation between satellite-derived soil moisture and NDVI was found in most areas of Australia's continent, with NDVI typically lagging behind soil moisture by one month, implying the influence of soil water availability on vegetation has a temporal scale dependence. More importantly, the integration of synchronous large-scale satellite-based observations of soil moisture and SIF contributes significantly to advances in the predictive understanding of global terrestrial coupled carbon-water cycles (Qiu et al., 2018).

The aims of this study were to evaluate varying responses of major dryland biomes to extreme wet events in terms of greenness (as measured by EVI) and photosynthesis (using SIF as a surrogate), incorporating in-situ eddy covariance flux data as a performance benchmark. In this way we aimed to attain new insights into the potential and limitations of spaceborne SIF over the xeric interior of Australia. Specifically, we address three scientific questions: (1) how are the temporal and spatial variations of SIF and EVI related to those of meteor-hydrological drivers under extreme wet pulses, (2) how do C3-dominated woodland (Mulga) and C4-dominated grassland (Hummock) differ in magnitude and rate of responses, (3) can SIF accurately track the dynamics of wet-induced dryland vegetation productivity (as measured by tower-based GPP).

2. Materials and methods

2.1. Study region

This study was conducted at a sub-continental scale over central Australia, encompassing an area of nearly 2.7 million km^2 between 18°S to 30°S and 120°E to 140°E (Fig. 1). This vast region receives mean annual precipitation ranging from 200 mm to 600 mm (Bureau of Meteorology, https://www.bom.gov.au) and is comprised with dominant vegetation types such as Hummock grassland, Mulga woodland, Mulga shrubland, Eucalypt woodland and Tussock grassland, covering 43.5 %, 11.6 %, 16.2 %, 7.7 %, and 6.6 % respectively. In this study, we note that categories of *Acacia* open woodlands and *Acacia* Forests and woodlands were reclassified as Mulga woodlands. The remaining woody (*Casuarina*, *Melaleuca* forests and woodlands, Mallee woodlands), shrub (Heathlands, Chenopod, Samphire shrublands, Forblands) and grass groups were sorted as Other Woodlands, Other Shrublands, and Other Grasslands separately (Fig. 1, Data source: National Vegetation Information System (NVIS), Major Vegetation Groups (MVGs), Version 5.1, https://www.environment.gov.au/).

Two eddy covariance tower sites within this extent, respectively are Alice Spring Mulga (AU-ASM, [22.28°S, 133.25°E]) and Ti Tree East (AU-TTE, [22.28°S, 133.64°E]) separated by approximately 40 km (http://www.ozflux.org.au/). The AU-ASM site is located in a Mulga woodland with a sparse canopy, while the AU-TTE site is in a *Corymbia* savanna containing scattered trees above a matrix of Hummock grass (Cleverly et al., 2016b). A detailed description of two sites concerning floristics, soil and landscape can be found in Eamus et al. (2016) and Cleverly et al. (2016b).

To examine variation in response to extreme wet events across vegetation types along with biome-specific vegetation-moisture relationships, we selected three relatively “pure” test-pixels at a 0.5° spatial resolution

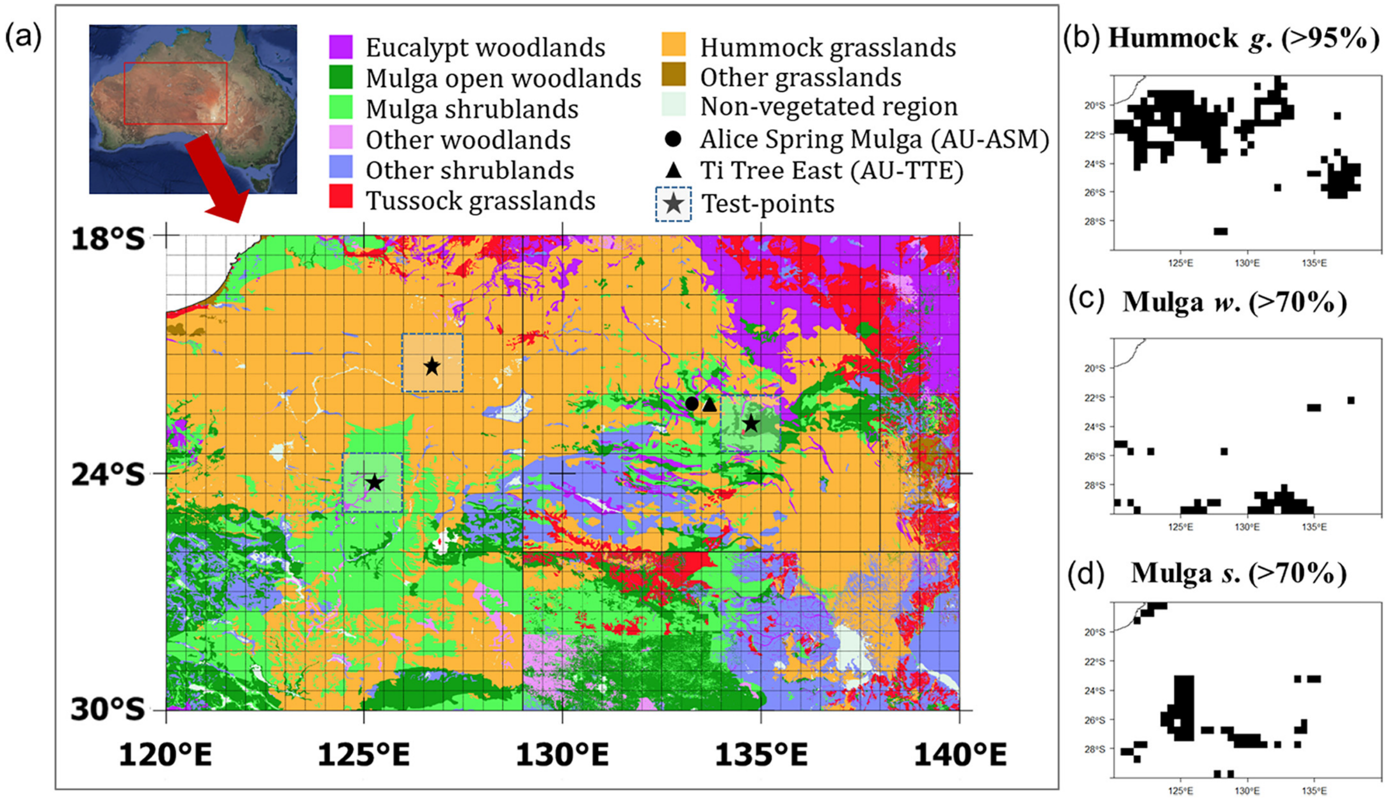

Fig. 1. (a) Map of reclassified major vegetation groups over central Australia (map source: NVIS Version 5.0). Black dot and triangle represent AU-ASM, AU-TTE flux tower sites respectively; Black pentagrams with the extent of the blue dashed square refer to the three selected test-points; Overlapped fishnet refers to a net of rectangular cells at 0.5° spatial resolution, consistent with the pixel size of GOME-2 SIF. The top-left figure displays the locations of the study area over the Australian continent (image source: Google Earth). (b, c, d) spatial distributions of relatively homogenous pixels of three major biomes at a 0.5° resolution. (g. refers to grassland, w. refers to woodland, s. refers to shrubland; the thresholds of selection percentages are listed in parentheses).

representing three major vegetation types (Hummock grassland, Mulga woodland, and Mulga shrubland). Pixel selection criteria: (1) given there was more Hummock grassland, pixels with coverage percent of Hummock grassland above 95 %, Mulga woodland & Mulga shrubland above 70 % based on NVIS MVGs were chosen; (2) As satellite variables were extracted within 3 × 3 window centered at test-points, pixels within the extent of 1.5° × 1.5° need to be covered by coherent vegetation type. The selected test-points are respectively TP-Hummock grassland [21.25°S, 126.75°E], TP-Mulga woodland [29.25°S, 132.75°E], and TP-Mulga shrubland [24.25°S, 125.25°E] (Fig. 1a).

2.2. Satellite data

EVI is an optimized version of vegetation index that effectively reduces soil background influences and is widely used as a proxy of canopy greenness (Huete et al., 2008). We used 11-years (2007–2017) of the Moderate Resolution Imaging Spectroradiometer (MODIS, Collection 6) MYD13Q1 (250 *m*, 16-day, tile: H30V11) and MYD13C2 EVI data set with climate modelling grid (0.05°, monthly) downloaded from NASA Earth Observation data (https://search.earthdata.nasa.gov/search). The equation of EVI is:

$$EVI = 2.5\frac{\rho_{NIR} - \rho_{red}}{\rho_{NIR} + 6\rho_{red} - 7.5\rho_{blue} + 1} \tag{1}$$

where ρ_{blue}, ρ_{red}, ρ_{NIR} are reflectance in the blue, red and near infrared bands respectively. To reduce noise and uncertainties, only the best quality data was selected in this study through removing pixels of which quality control flag of the first 2 bits neither 00 nor 01. The monthly EVI at 0.05° resolution was spatially aggregated into 0.5° resolution for further comparison with GOME-2 SIF.

Spaceborne SIF data in this study were retrieved from GOME-2 onboard the European Organisation for the Exploitation of Meteorological Satellites (EUMETSAT) Meteorological Operational A and B platforms (MetOp-A, and MetOp-B) launched on 19 October 2006 and 17 September 2012, respectively (Joiner et al., 2014). The GOME-2 instrument is a nadir-scanning spectrometer, which measures at around 9:30 local equator crossing time, and it has a relatively large footprint (approximately 40 km × 80 km at nadir, before 15 July 2013, and 40 km × 40 km since 15 July 2013) (Joiner et al., 2013, 2014; Köhler et al., 2015). GOME-2 comprises four main optical channels with the spectral range from 240 to 790 nm, and the fourth channel ranges between 590 and 790 nm with a spectral resolution of approximately 0.5 nm and a relatively high signal-to-noise ratio (Joiner et al., 2013; Song et al., 2018). This dataset is primarily retrieved from the filling-in of solar Fraunhofer lines in the vicinity of the 740 nm far-red fluorescence emission peak, based on a simplified radiative transfer model in the company of a principal component analysis in order to disentangle the fluorescence signals from atmospheric absorption and surface reflectance (Joiner et al., 2013; Köhler et al., 2015). This dataset is a retrieval of the far-red chlorophyll fluorescence peaking at 740 nm, based on a simplified radiative transfer model in the company of a principal component analysis (Joiner et al., 2013; Köhler et al., 2015). Two sets of SIF records were used in this study: (1) more than twelve years (from February 2007 to March 2019) of monthly SIF data at a spatial resolution of 0.5° (Level 3, version 28, based on GOME-2 from MetOp-A, denoted as **GOME-2A**); (2) six years (from March 2013 to March 2019) of monthly SIF (Level 3, version 28, based on GOME-2 from MetOp-B, denoted as **GOME-2B**). Both GOME-2 SIF datasets were obtained from the National Aeronautics and Space Administration (NASA) Goddard Space Flight Centre (https://avdc.gsfc.nasa.gov/pub/data/satellite/MetOp/GOME_F/v28/). Although various filtering is applied, there still exists negative value due to imperfect bias correction and noise (Joiner et al., 2013).

Monthly soil moisture (SM) at 0.25° spatial resolution was downloaded from the European Space Agency (ESA) Climate Change Initiative (CCI, version 4.4) data portal (http://www.esa-soilmoisturecci.org). This dataset merges active microwave with passive microwave soil moisture products through a harmonization approach to represent surface soil moisture (Chen et al., 2014b). Satellite-based precipitation dataset from Tropical Rainfall Measuring Mission (TRMM) Multi-satellite Precipitation Analysis mission was utilized with monthly 0.25° resolution (3B43, Level 3, version 7) downloaded from NASA Precipitation Processing System (https://pps.gsfc.nasa.gov/). Moisture-related variables were spatially aggregated into 0.5° resolution, consistent with the GOME-2 SIF record for further analysis.

2.3. Eddy covariance data

The original Level 5 (AU-TTE, Net Ecosystem Exchange - NEE, ranging from 2012 to 2017) and Level 6 data (AU-ASM, hourly GPP, ranging from 2010 to 2017) provided by the OzFlux network (http://www.ozflux.org.au/) were used to pre-process, including quality control assessment, removal of outliers, and gap-filling (Cleverly et al., 2013a, 2013b). The R package, REddyProc (Wutzler et al., 2018), was implemented for Level 5 data to estimate daily mean GPP with hourly eddy covariance and meteorological data. This tool used the gap-filling and flux partitioning algorithms to partition Level 5 data (NEE) into GPP and field ecosystem respiration (Reichstein et al., 2005), conducted in open-source R scientific computation environment (Version 3.5.1). The estimated daily GPP were aggregated into monthly GPP to match with satellite-based observations.

2.4. Wet intensity classification

Owing to the strong seasonality of rainfall (wet season: November–April), monthly anomalies of precipitation were calculated as a deviation from their corresponding multiyear (2007–2017) mean for each month. We used the hydrological year from July to next June to account for the location of the study region in the South Hemisphere. Two extreme wet periods were analyzed: (a) from February 2010 to March 2011, and (b) from December 2016 to January 2017. Cumulative precipitation anomalies (CPA) representing the accumulated amount of precipitation increment during the periods of wet pulse were computed for each grid cell. Wet intensity defined by CPA was classified into five categories including *Extreme wet, Severe wet, Intense wet, Moderate wet,* and *Dry* (Table 1).

2.5. Statistics

With the purpose of wet-related signal detection, monthly anomalies of each vegetation variable (*XAnomaly*) were calculated as a deviation from their corresponding multiyear (2007–2017) mean for each month. To further account for spatiotemporal variability leading to diverse influences on vegetation response (Vicente-Serrano et al., 2013), we applied standardized anomalies (SA) of all variables over each grid cell for further examination of moisture-vegetation relationships across space and time. Standardized anomalies, calculated by dividing anomalies by the climatological standard deviation, generally provide more information about the magnitude of the anomalies because influences of dispersion have been removed (Dabernig et al., 2017). The equation is:

$$SA_{ij} = \frac{X_{ij} - \overline{X_j}}{\sigma_j} \tag{2}$$

where *i* is the yearly temporal coverage from 2007 to 2017, *Xij* is the monthly ranging from July to next June, $\overline{X_j}$ and *σj* are the mean and standard deviation of time series *x* at month *j*. In order to contrast the performance between GOME-2A and GOME-2B, relative anomalies (RA) calculated as a departure from the multiyear mean and divided by the multiyear mean were also implemented for two SIF datasets. The equation is:

$$RA_{ij} = \frac{X_{ij} - \overline{X_j}}{\overline{X_J}} \tag{3}$$

where *i* is the yearly temporal coverage from 2014 to 2019, *Xij* is the monthly ranging from July to next June, $\overline{X_j}$ is the mean of time series *X* at month *j*.

We assessed the relationship between hydro-meteorological and vegetation variables over three test sites at monthly scale by calculating the coefficient of determination (r^2). A *t*-test was utilized to examine the statistically significant level of the relationships (*p-value*). To quantify the temporal response of vegetation to water availability along with comparison of SIF-EVI per each biome, pixel-wise Pearson's correlation coefficient (*R*) between SM and SIF, as well as SM and EVI within finite time lags analysis (0–6 months) was examined by shifting vegetation variables one month forward at a time across a domain.

From a perspective of validation of satellite observations, SIF, EVI, GPP series were respectively scaled into a decimal between 0 and 1 by min-max normalization. Subsequently, the correlations of tower-based GPP and satellite-based SIF, EVI were evaluated using the coefficient of determination (r^2) and linear regression slope (*k*) separately during wet years (2010–2011, 2016–2017) and normal year mean (2012–2016). The purpose of the min-max normalization, which does not alter the strength of correlations, is to inter-contrast the regression slopes between GPP-SIF and GPP-EVI. Given a huge mismatch between the footprint of flux tower and satellite observation, especially for spatially coarse SIF, we reviewed the coefficient of determination between multi-year series (2010–2017) of GPP and EVI at a variety of satellite-observed footprints increasing from 0.25 *km* to ~450 *km*, along with the relationship between multi-year series of EVI and SIF, GPP and SIF.

3. Results

3.1. Wet pulse characteristics in 2010–2011 and 2016–2017

Spatially averaged seasonal variations in precipitation, SM, EVI, and SIF during wet pulse years (2010–2011, 2016–2017) and climatology (non-wet years mean) are shown in Fig. 2. It was found that precipitation was sustained during both wet pulses for two months, occurring in late summer/early autumn of 2011 (Feb-Mar) and the hot summer of 2016–2017 (Dec-Jan), in which rainfall was over 3 standard deviations (SD) larger than the non-wet year mean (Fig. 2a). Soil moisture exhibited similar temporal trajectories, reaching the peak almost simultaneously with precipitation, although high soil water content was maintained above the climatology (>1 SD larger) after extreme wet periods, especially in 2010–2011 (Fig. 2b). The seasonal amplitude of EVI in both wet years was pronouncedly enhanced relative to the multi-year mean, particularly during the extreme wet and post-wet periods (Fig. 2c). Correspondingly, SIF exhibited markedly enlarged seasonal patterns in both wet years compared with climatology, especially the maximum in 2010–2011 which exceeded 2 SD larger than the peak of 2016–2017 (Fig. 2d). Throughout the post-wet period of both wet years, SIF declined sharply after climaxing, similar to

Table 1
Summary of wet pulse intensity classification.

CPA (mm)	Wet level
(>300)	Extreme wet
(200,300]	Severe wet
(100,200]	Intense wet
(0,100]	Moderate wet
(<0]	Dry

CPA = Cumulative Precipitation Anomaly, calculated using TRMM rainfall data for every pixel during the wet pulse periods (2010–2011: February~March; 2016–2017: December~January), and representing the accumulated amount of precipitation increment during the periods of wet pulse.

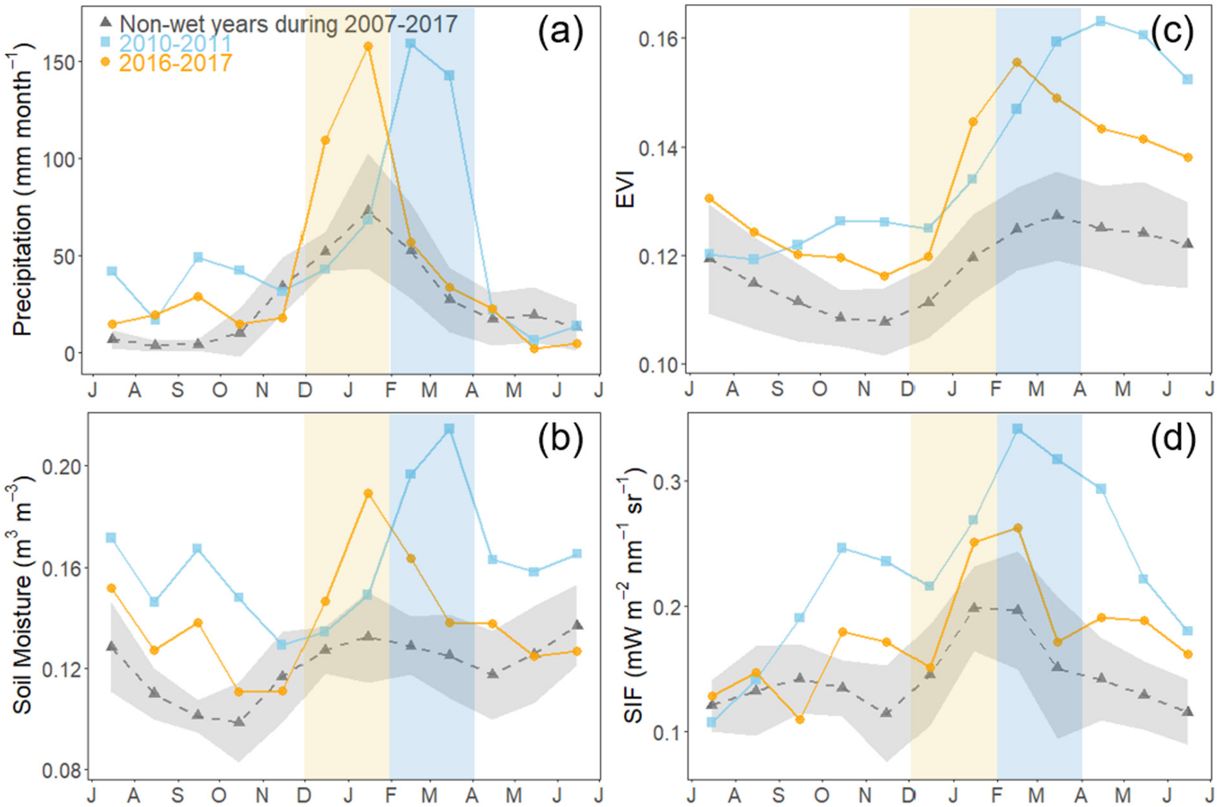

Fig. 2. The region-wide mean seasonal cycle of monthly (a) precipitation, (b) soil moisture, (c) EVI, and (d) SIF over study area during 2010–2011, 2016–2017 and non-wet years. The shaded area represents ± 1 standard deviation (σ). The vertical rectangles refer to extreme wet periods of 2010–2011 (yellow) and 2016–2017 (blue) respectively.

the temporal trajectory of rainfall. By contrast, EVI displayed a more gradual decrease, corresponding with soil moisture.

Spatiotemporal distributions of standardized anomalies of precipitation, soil moisture, SIF, and EVI during wet pulses and the subsequent three months of 2010–2011 and 2016–2017 are presented in Figs. 3 and 4, respectively. Across roughly the whole study region (over 95 %), precipitation and SM showed predominantly positive anomalies (SA > 0) and exhibited congruent spatial patterns during the extreme wet period from February to March of 2010–2011 (Fig. 3a, b). Afterwards, two hydrometeorological variables varied at the post-wet stage in which SM within the majority of area (over 93 %) remained positive anomalies in contrast to over half region of precipitation dropping below average (SA < 0). Overall, SIF*SA* and EVI*SA* tended to be spatially consistent with SM*SA*, where both vegetation variables within the majority of domain (82 % for SIF*SA* and 96 % for EVI*SA*) were larger than average (Fig. 3c, d). In particular, EVI within 75.3 % of the study area maintained considerably positive anomalies (SA > 1) since March 2011; however, the percentages of SIF*SA* above 1 reduced from 48.5 % to 29.4 %.

By contrast, precipitation and SM in the 2016–2017 wet pulse (Dec-Jan) were also larger than average (SA > 0) across the most region (~90 % for Precip*SA* and ~ 98 % for SM*SA*, shown in Fig. 4a, b); however, these anomalies were not as large as those in 2010–2011. The percentages of SA > 2 in 2010–2011 were over 40 % for both hydro-meteorological variables relative to 32.3 % for Precip*SA* and 18.1 % for SM*SA* in 2016–2017 wet pulse. EVI displayed positive anomalies over most regions (95.8 %) since January 2017 (Fig. 4d), whereas SIF*SA* exhibited a spatial pattern of which over nearly half region (44.7 %) was below than average (SA < 0) throughout 2016–2017 wet pulse as well as following three months (Fig. 4c). Additionally, SIF was significantly positive (SIF*SA* > 1) over <23 % of the region, as contrasted to 73.9 % of EVI (EVI*SA* > 1).

Region-wide maps of wet intensity as measured by cumulative precipitation anomalies during the 2010–2011 and 2016–2017 wet pulses were generated (Fig. 5a, b). The wet pulse of 2010–2011 wherein the majority of the region experienced intense rainfall anomalies (Wet level ≥ 2) was a more intense event relative to that of 2016–2017. Additionally, extreme rainfall anomalies (Wet level ≥ 3) mainly occurred in the northeast as well as a patch of the southwest in the first wet pulse (2010 – 2011), relative to the northwest between 121°E-127°E and 19°S-23°S in the later wet event (2016–2017). The percentages of each wet level in both wet pulses are illustrated along with three dominant vegetation types (Fig. 5c, d). Only 17.1 % of major biomes in 2016–2017 underwent severe or extreme wet situation (Wet level ≥ 3), mainly occurring over Hummock grasslands, in comparison to 36 % of those in 2010–2011, comprising 11.3 % of Mulga woodlands and Mulga shrublands.

3.2. Response of vegetation per biome type

Seasonal profiles of anomalies of EVI and SIF in 2010–2011 and 2016–2017 for three major biomes are depicted in Fig. 6. The magnitude of EVI*Anomaly* and SIF*Anomaly* for Mulga woodlands increased remarkably with increasing wet intensity (Fig. 6c, d, i, j), and both vegetation indicators of that in 2010–2011 showed the largest positive anomalies in severe wet (Wet level = 3) among all categories (Fig. 6c, d). Contrarily, the enhancement of $\mathrm{SIF}_{Anomaly}$ and $\mathrm{EVI}_{Anomaly}$ for Hummock grasslands and Mulga shrublands was apparently not as large as those for Mulga woodlands and generally constant when the amount of cumulative rainfall anomalies exceeded 100 mm (Wet level ≥ 2) in both wet years. During the 2016–2017 wet pulse, SIF of Hummock grasslands was continuously close to the average ($\mathrm{SIF}_{Anomaly} \sim 0$), even under the extremely wet situation (Wet level ≥ 3, Fig. 6h). Likewise, the later wet event (2016–2017) marginally raised the amplitude of $\mathrm{EVI}_{Anomaly}$ of Hummock grasslands (Fig. 6g). In addition, $\mathrm{EVI}_{Anomaly}$ of all major biomes sustained positive and decreased gradually after extreme wet periods of both wet events, in contrast to the rapid decline of $\mathrm{SIF}_{Anomaly}$.

To further investigate the relationship between moisture condition and vegetation function, temporal dynamics of precipitation, soil

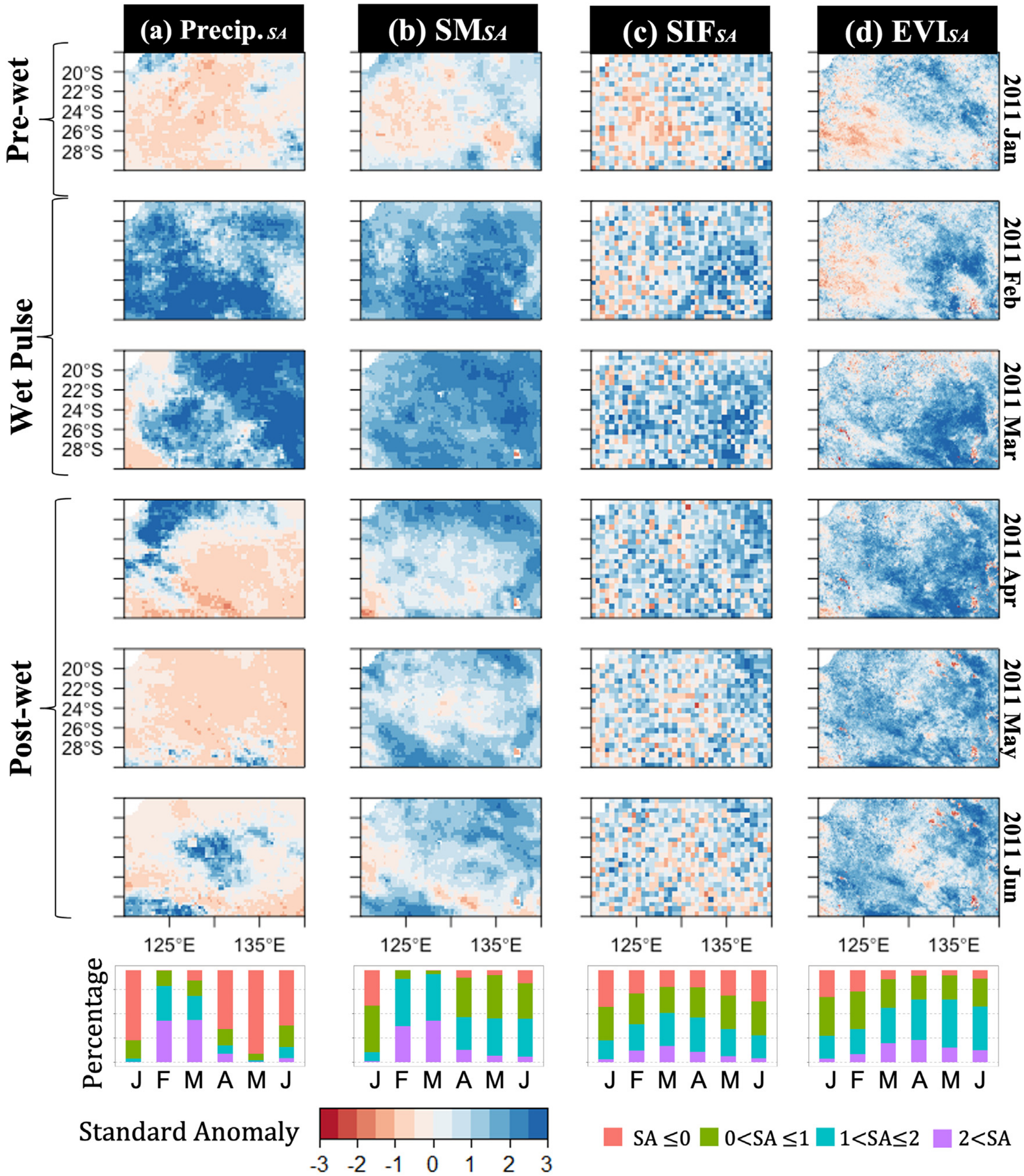

Fig. 3. Spatial patterns of standard anomalies of (a) precipitation, (b) soil moisture, (c) SIF, and (d) EVI during 2010–2011 wet pulse as well as following three months. The bottom panel shows the frequency map of each SA (standard anomaly) category of the corresponding variable during the six months (J: January; F: February, M: March; A: April; M: May; J: June).

moisture, SIF, EVI over three selected pixels in 2010–2011 and 2016–2017 are depicted in Fig. 7. In general, both vegetation variables of all three test-points were more tightly correlated with soil moisture (r^2 ranging from 0.44 to 0.66, $p < 0.05$) than precipitation (r^2 ranging from 0.01 to 0.68). According to seasonal trajectories of SIF in two wet years, the peak of the growing season of all three test-points is almost simultaneous or up to one-month lag behind the timing of maximum precipitation and soil moisture. For TP-Mulga woodland, the peaks of growing season based on EVI also coincided with the peaks of precipitation and soil moisture during the periods of wet pulses in both years (Fig. 7b, e). By contrast, the peak of EVI at TP-Hummock grassland and TP-Mulga shrubland exhibited more than one-month lagging (1–4 months) relative to the peak of water-related drivers (Fig. 7a, c, d, f). Although rainfall declined rapidly since February 2017, both SIF and EVI at TP-Hummock grassland remained increasing in the following four months (Feb-May) on a basis of a gradual decrease in soil moisture (Fig. 7d).

Fig. 8a presents the boxplots of pixel-wise Pearson's correlation coefficients between 11-year series of monthly SM and EVI or SIF among three major biomes. Satellite-based soil moisture can satisfactorily ($p < 0.01$) explain seasonal and inter-annual variation in EVI for all major biomes (R ranging from 0.4 to 0.8), relative to less pronounced relevance with SIF (R ranging from 0 to 0.5). Apart from this, relationships between SIF and SM in biomes with larger SD, especially among Hummock grassland and Mulga shrubland, tended to be more spatially variable (Fig. 8a). In contrast to Hummock grassland and Mulga shrublands, EVI in Mulga woodland with minimum time lags (Lags ≤ 1) was most sensitive to soil moisture availability, whereas SIF exhibited proportional percentages of time lags (Lag: 0–3)

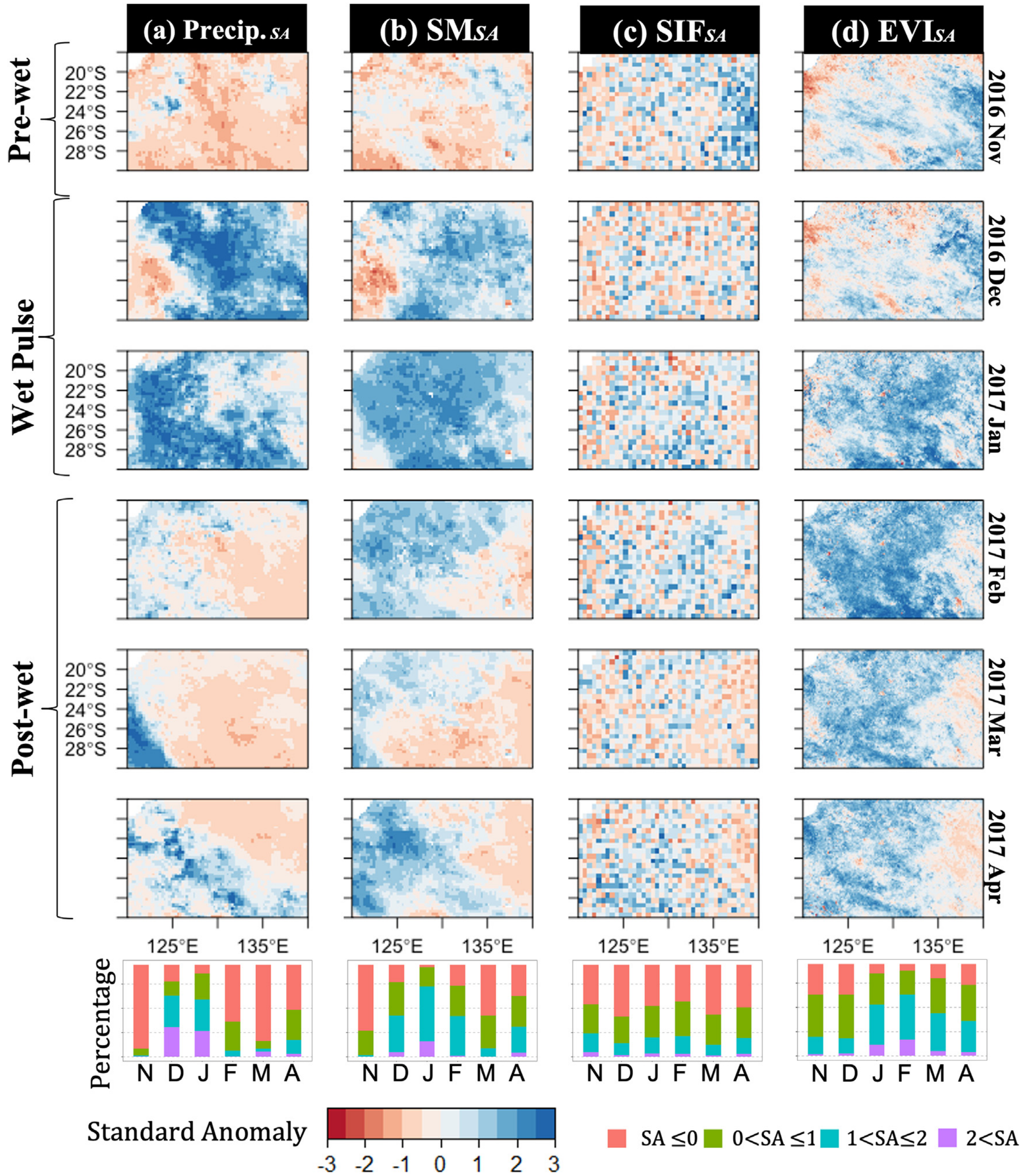

Fig. 4. Spatial patterns of standard anomalies of (a) precipitation, (b) soil moisture, (c) SIF, and (d) EVI during 2016–2017 wet pulse as well as following three months (N: November; D: December; J: January; F: February, M: March; A: April).

for three major biomes (Fig. 8b), representing there are smaller biome-specific differences in the relationships between SM-SIF relative to those between SM-EVI. Regarding SIF within 17.8 % of Hummock grasslands showing simultaneous response (Lag = 0), roughly all EVI of Hummock grassland (~99 %) were lagging one month or more behind soil moisture. For the majority of pixels with larger time lags (Lag ≥3), there were generally weak and insignificant correlations between soil moisture and SIF ($R <$ 0.2, $p >$ 0.01).

3.3. SIF-EVI-GPP relationship

Multi-year time series of normalized tower-based GPP, satellited-observed SIF and EVI over AU-ASM and AU-TTE are shown in Fig. 9a,b. Relative to seasonal trajectories in non-wet years, both extreme wet events substantially raised the seasonal amplitude of GPP, EVI and SIF at the two flux tower sites. The peak of productivity of AU-ASM in 2016–2017 (GPP_{norm} = 1; GPP_{max} = 129.4 gC m^{-2} mo^{-1}) slightly exceeded that in 2010–2011 (GPP_{norm} = 0.89; GPP_{max} = 114.9 gC m^{-2} mo^{-1}) as well as that of AU-TTE in 2016–2017 (GPP_{max} = 116.3 gC m^{-2} mo^{-1}). As compared with highly fluctuated time series of SIF signals over both sites, reflectance-based vegetation index (EVI) exhibited likewise interannual and seasonal variation in tower-based GPP on the whole.

We found enhanced correspondence between GPP and SIF (r^2: 0.76, 0.62, and 0.85), GPP and EVI (r^2: 0.74, 0.91, and 0.6) in wet years relative to non-wet years (r^2: 0.44, 0.43, 0.59, and 0.71) for both AU-ASM and AU-TTE (Fig. 9c-f). Furthermore, the linear regression between GPP and two satellite-based variables in 2010–2011 and 2016–2017 (k ranging from 0.85 to 1.03) were closer to 1:1 diagonal, compared with those in the non-wet year (k ranging from 0.63 to 0.82), representing that satellite observations can more accurately capture dryland vegetation production in

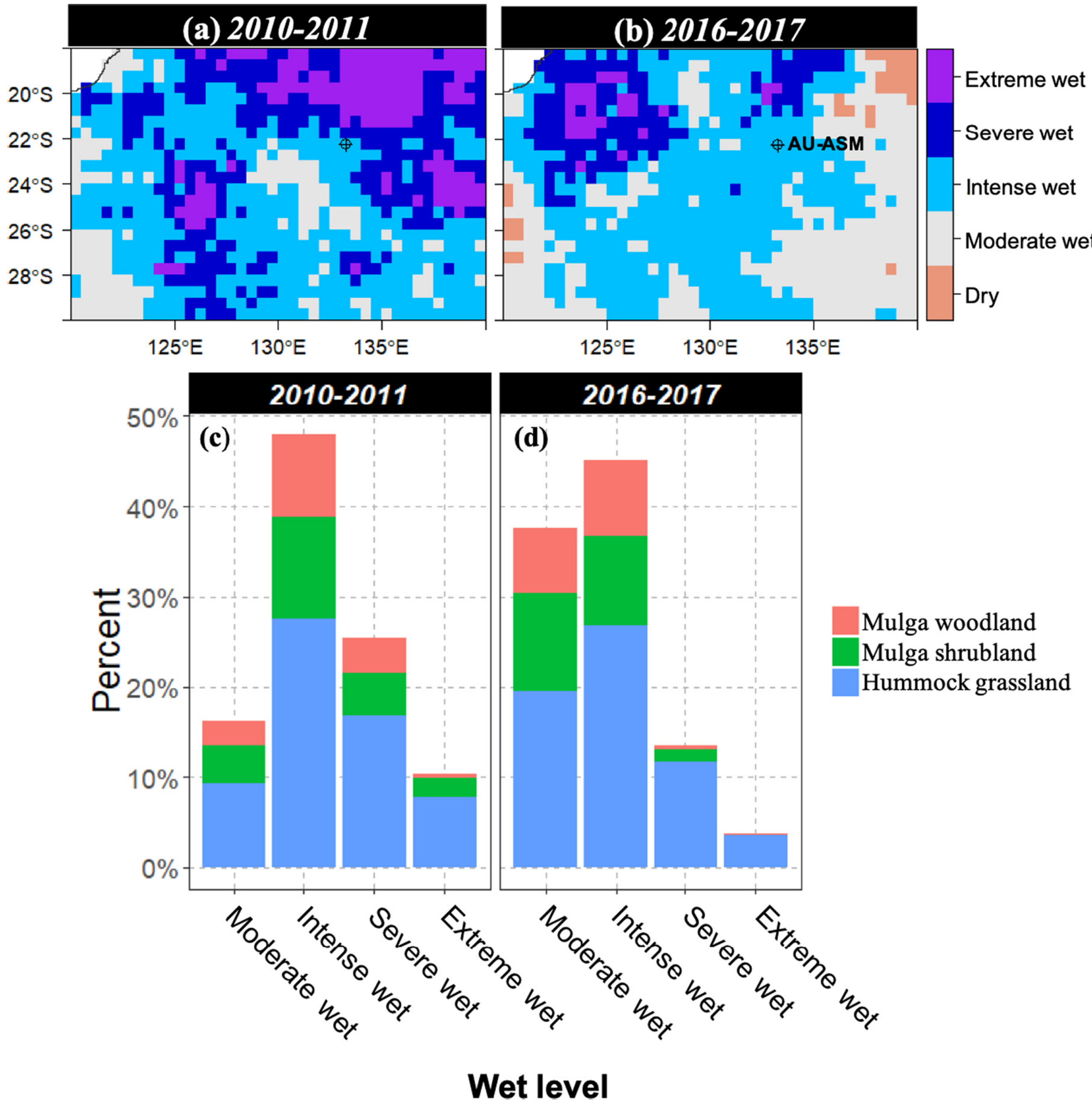

Fig. 5. (a, b) Spatial pattern of wet intensity as measured by Cumulative Precipitation Anomalies during 2010–2011 and 2016–2017 wet pulses; (c, d) percentages of each wet level over three major vegetation types.

wet years ($k \cong 1$), however, tend to be an underestimation under non-wet climatic scenarios ($k < 1$).

To examine the impact of mismatch footprint between flux tower measurement and satellite observation, relationships between multi-year series of GPP and vegetation variables are summarized with respect to a range of spatial resolution from 0.25 km to ~450 km (Fig. 10). The correlations between GPP and EVI at AU-ASM were generally constant with increasing footprints of satellite observations from 0.25 km to 35 km (r^2 ranging from 0.6 to 0.62) as a result of the tower site located in an extensive homogeneous Mulga woodland. Those were consistently stronger than correlations between GPP and EVI at AU-TTE (r^2 ranging from 0.38 to 0.53), which is located in a heterogeneous landscape. Subsequently, relationships at both sites decreased along with the footprints arising from 5 km to 45 km, especially for AU-TTE (r^2 declined from 0.53 to 0.4). At a 0.5° spatial resolution of SIF data, correlations of SIF and EVI, SIF and GPP at two sites analogously increased and then decreased in conjunction with the extending size from 50 km to 450 km. The synchronous trajectories of correlations along with increasing footprints of SIF observations across both sites are owing to the fact that there are increasing overlapped footprints (percentage of overlapped area > 66 %) since spatial coverage of ~150 km on the basis of AU-ASM and AU-TTE located in two adjacent pixels (GOME-2 SIF grid).

4. Discussion

4.1. Spatiotemporal response to extreme wet pulse

Both extreme wet pulses greatly promoted the seasonal amplitude of SIF and EVI in comparison with non-wet years mean (Fig. 2). Resembling seasonal profiles between hydro-meteorological and vegetation variables in both wet years implies that hydro-climatic variation exerts an impressive influence on vegetation dynamic across the xeric interior of Australia, congruent with previous studies (Andrew et al., 2017; Chen et al., 2014a; Cleverly et al., 2016b; Yang et al., 2014). In particular, EVI and SIF almost synchronously and rapidly reacted to increasing moisture, although they varied in their response during the post-wet period (Figs. 2, 3). Our findings that EVI followed a gradual decline following the wet period relative to the swift decline of SIF were also consistent with other studies, illustrating much slower chlorophyll degradation than the reduction in photosynthesis (Jenkins et al., 2007; Ma et al., 2013).

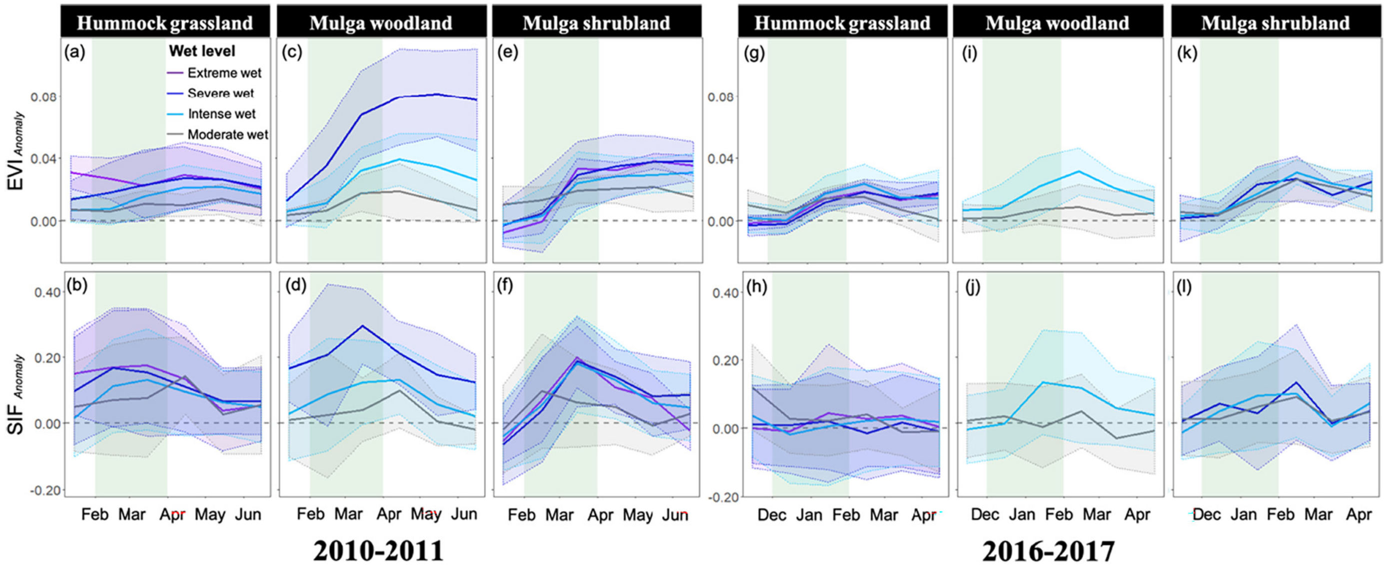

Fig. 6. Seasonal variation in spatial averaged anomalies of EVI and SIF of major biomes by each wet level in 2010–2011 (a-f) and 2016–2017 (g-l); Colorful areas represent ± 1 standard deviation of the corresponding wet level. The shaded rectangles refer to extreme wet periods.

Unlike the corresponding spatiotemporal evolution of EVI and SIF in the first wet event (Fig. 3), two vegetation variables in the 2016–2017 wet pulse exhibited inconsistent trends, of which EVI showed considerably positive anomalies across almost the entire domain, by contrast to the patchy spatial pattern of SIF*SA* (Fig. 4). This result reveals that water availability may not be the only limiting factor for vegetation photosynthesis in semi-arid ecosystems under the extreme wet scenario, in addition to the occurrence of later wet pulse in hot summer (Dec-Jan-Feb). There is evidence

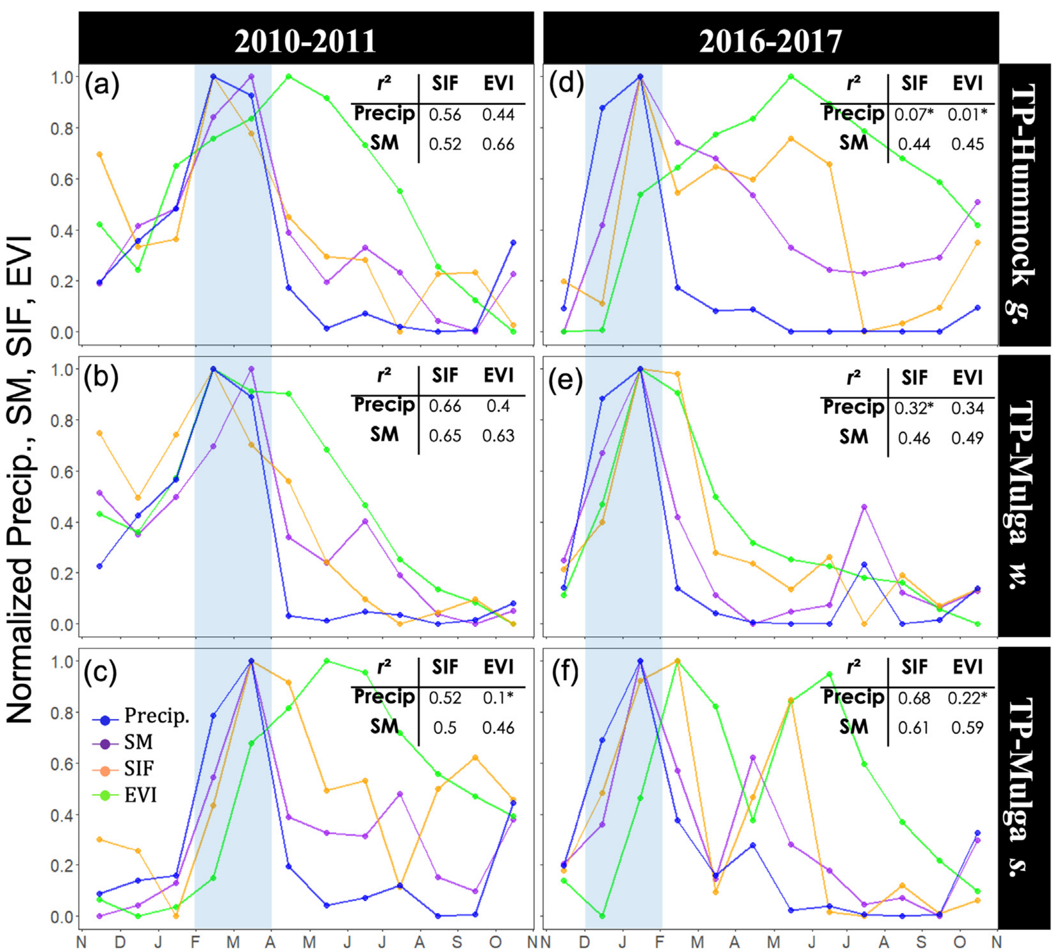

Fig. 7. Temporal dynamics of precipitation, soil moisture, SIF, EVI over three selected pixels in (a, b, c) 2010–2011 and (d, e, f) 2016–2017. Inserted charts show the coefficient of determination (r^2) between climatic drivers and vegetation variables. (*: *p*-value >0.05).

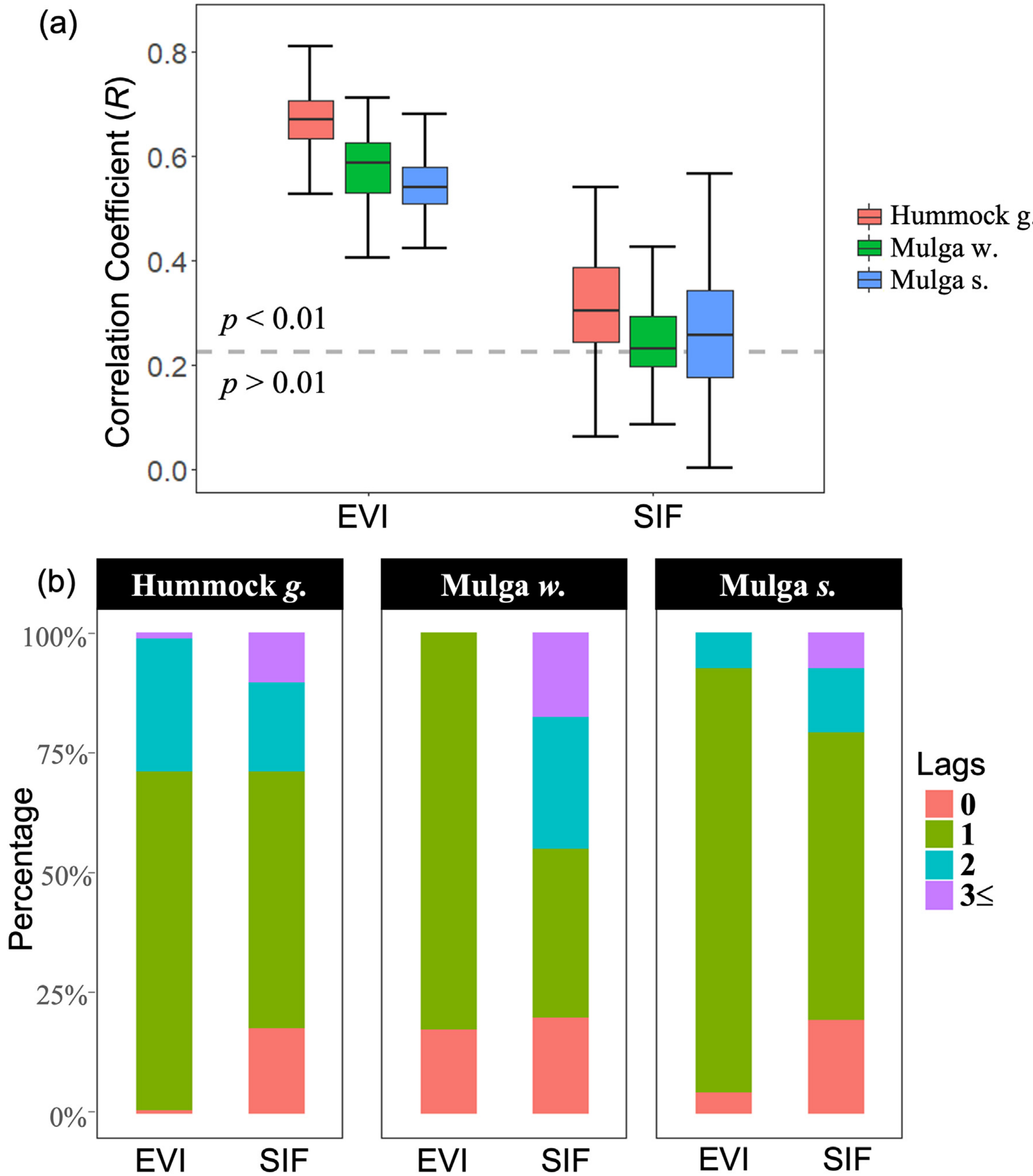

Fig. 8. Relationship between soil moisture and EVI, SIF (a) Boxplot of correlation coefficients between monthly Soil Moisture and EVI, SIF during 2007–2017 along with (b) the corresponding time lags (months). Above the dashed line represents p-value below 0.01 and vice versa. (g. refers to grassland, w. refers to woodland, s. refers to shrubland).

that, on a seasonal basis, the primary drivers of vegetation productivity in an Australian tropical savanna were soil moisture in the dry season and solar radiation in the wet season, respectively (Moore et al., 2018).

Apart from the above-average photosynthetically active radiation in 2016–2017 wet pulse, another feasible reason causing divergent responses between SIF and EVI is the degradation of GOME-2A instrument after operating over 11 years giving rise to the loss of signal-to-noise ratio, especially over low-productivity region (Dikty et al., 2011; Geruo et al., 2017; Zhang et al., 2018). Through evaluating the performance of SIF derived from GOME-2A as compared with much less degraded instrument GOME-2B, both SIF records exceeded 1 SD larger in 2016–2017 wet pulse relative to the multi-year mean (2014–2019) (Fig. S1). Further, the strength of the correlations of the two SIF datasets compared with tower-based GPP was significantly strong (GOME-2A: R = 0.68–0.72; GOME-2B: R = 0.68–0.7; $p < 0.001$), demonstrating that both instruments have the comparable capability for monitoring the seasonal and interannual dynamic of dryland vegetation in recent years (Fig. S2). This result implies that any degradation issue of GOME-2A would play a secondary role on the lower responsiveness in SIF signals, relative to EVI, in the 2016–2017 wet pulse.

There is a notable difference in the temporal response between SIF and EVI in both wet years (Fig. 7). Following the precipitation pulse triggering rapidly increasing soil water content, SIF swiftly responded and reached the climax ahead of EVI among different vegetation types (Fig. 7). It is also evident that another small peak of soil moisture in April 2017 over TP-Hummock resulted in a rapid response of SIF prior to that of EVI (Fig. 7f). Results suggest that SIF tended to be a more prompt indicator of dryland vegetation response to changes in hydro-climatic conditions, although SIF exhibited an insignificant relationship with soil moisture due in part to

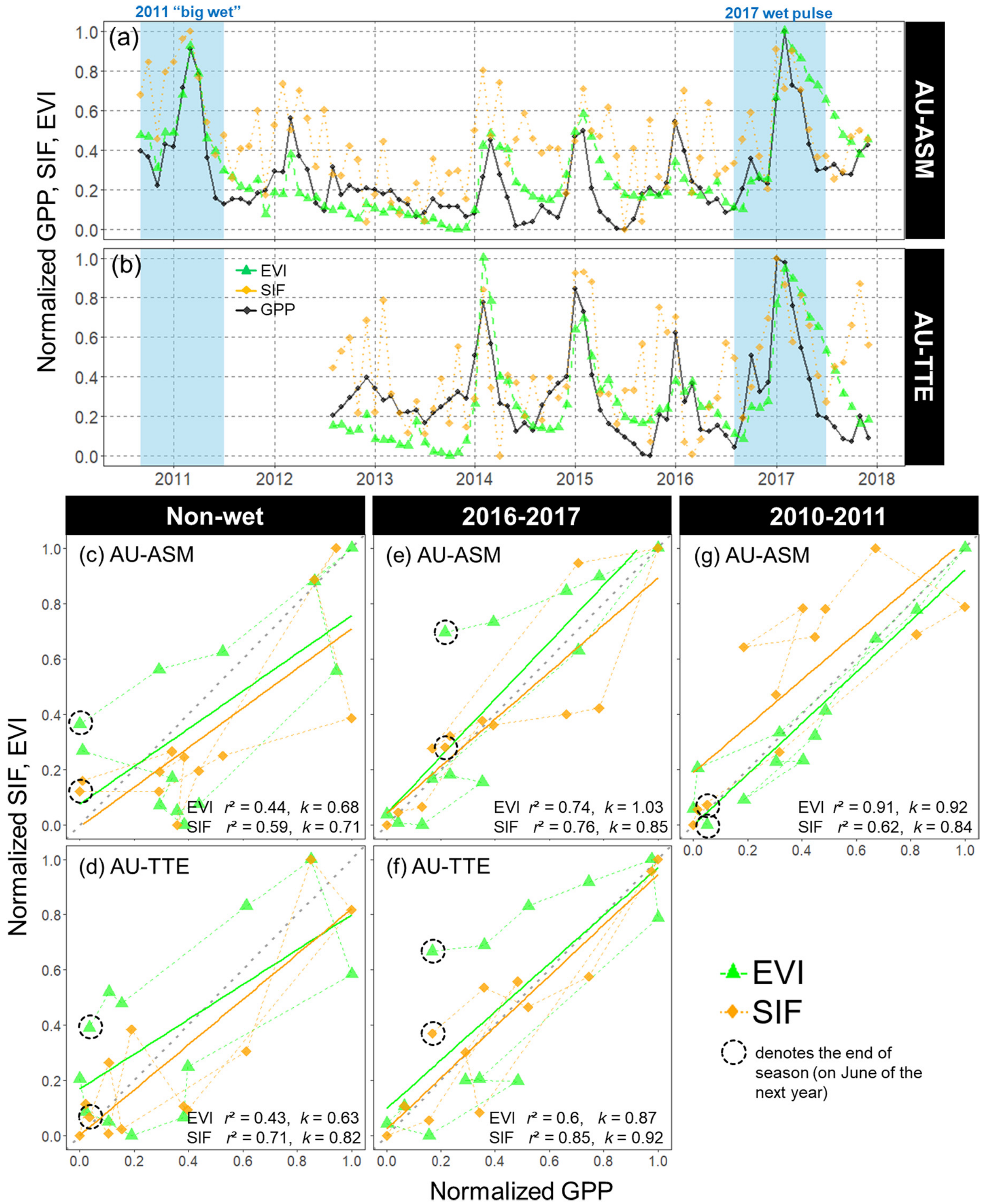

Fig. 9. Comparison of satellite observations and tower-based measurements. (a, b) Multi-year time series of normalized GPP, SIF, and EVI over AU-ASM and AU-TTE at monthly scale; (c-g) relationship between normalized GPP and SIF, EVI over flux tower sites during wet pulse years (2010–2011, 2016–2017) and non-wet year mean (2012–2015). Points followed by seasonal time series are connected with dashed line. Black dashed circle refers to the value at the end of hydrological year (in June). Coefficient of determination (r^2) and the slope of linear regression (k) between normalized GPP and normalized SIF, EVI are shown at the bottom-right of each panel.

the high fluctuations in the SIF time series retrieved from satellite observations (Fig. 8).

4.2. Sensitivity of Mulga and Hummock grass to water availability

Responses of dryland vegetation to rainfall pulses depend on receipt of sufficient water to trigger a response (Cleverly et al., 2013a). In addition, discrepancies in photosynthetic capacity between C3-dominated Mulga and C4-dominated Hummock grasses dictate the timing and strength of an ecosystem photosynthetic response (Barron-Gafford et al., 2012). Regardless of the duration of both wet events persisting for two months, they differed in timing, magnitude and extent, in which extreme rainfall anomalies of 2016–2017 mainly occurred over Hummock grasslands, in contrast to that of 2010–2011 involving most vegetation types with extended coverage (Fig. 5). At a given wet intensity, Mulga woodland with an invariably larger amplified magnitude of both EVI*Anomaly* and

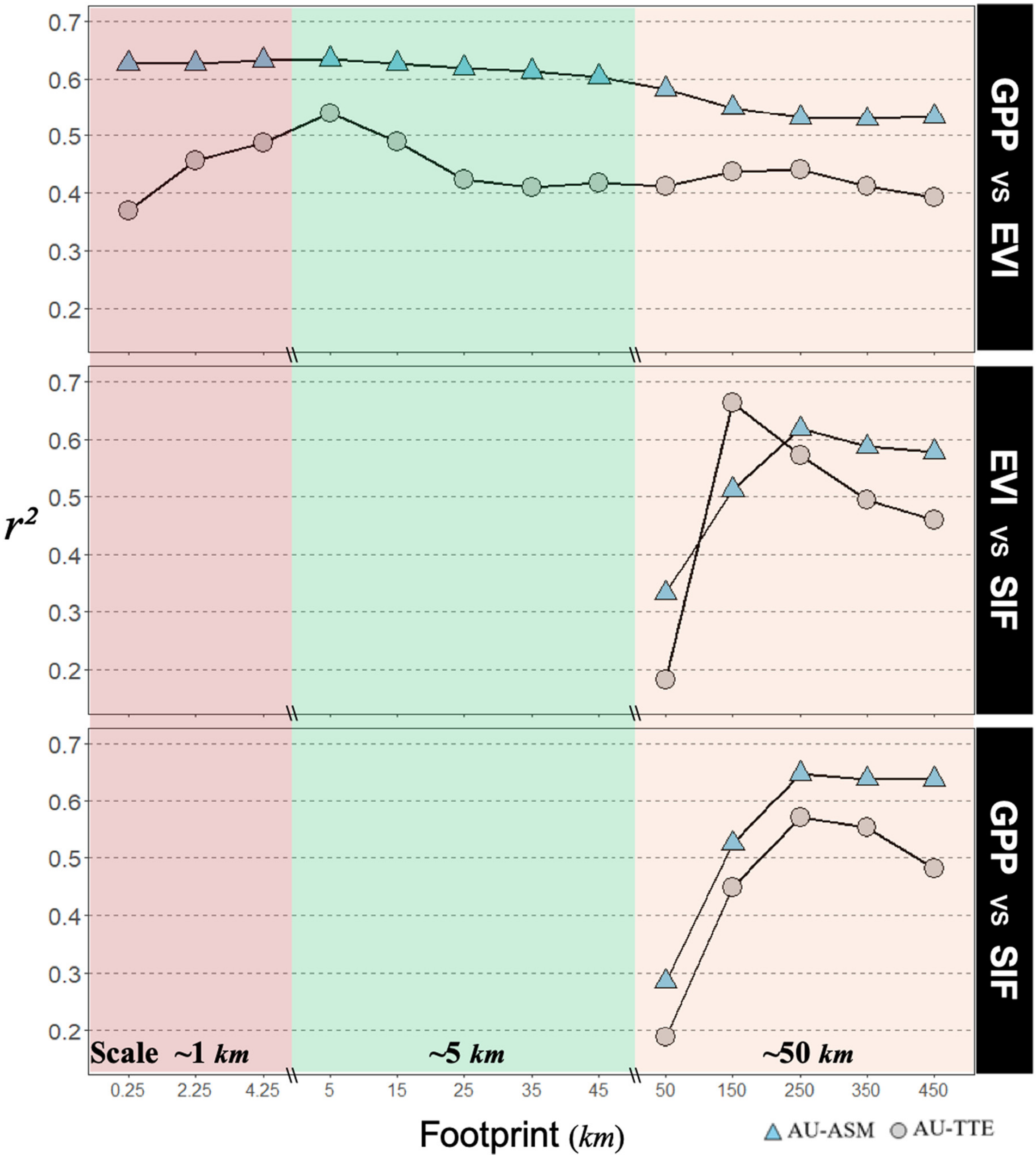

Fig. 10. Coefficients of determination between multi-year series of tower-based GPP and EVI, EVI and SIF, GPP and SIF at a range of spatial resolution from 0.25 km to ~500 km.

SIF*Anomaly* was most responsive among major biomes (Fig. 6). The greenness of Mulga woodlands tended to be consistently more sensitive to soil moisture availability, with larger slopes (*k*) and smaller time delays (Figs. 7, 8) than for other biomes, indicating that the rate of chlorophyll accumulation of Mulga is faster than that of Hummock grasslands. SIF of three major biomes exhibited comparable sensitivity, with almost equal slopes and analogously proportional time lags, despite weaker correlations. Compared with EVI, the majority of the SIF signal also lagged behind soil moisture, congruent with previous findings in central Australia (Detmers et al., 2015). Through inter-comparing between two SIF records derived from GOME-2A and GOME-2B among three major biomes (Fig. S3), we found that both SIF in Mulga woodlands exhibited the largest positive anomalies (RA: 1–2) in 2016–2017 wet pulse relative to an alternative baseline (2014–2019) as compared with those in Hummock grasslands (RA < 1), although extreme and severe rainfall anomalies in 2016–2017 mainly occurred over Hummock grasslands. The results again demonstrate that less responsiveness of SIF in 2016–2017 (relative to that in 2010–2011) is mainly owing to the less sensitivity of Hummock grasslands (relative to Mulga woodlands) to surplus water availability, instead of decreasing trend in SIF signals derived from GOME-2A.

Soil moisture, rather than precipitation, could explain most vegetation variations both seasonally and interannually (Figs. 7, 8), reflecting that satellite-observed soil moisture can be an effective indicator of dryland vegetation growth (Nicolai-Shaw et al., 2017; Qiu et al., 2018). Chen et al. (2014b) reported that satellite-derived soil moisture was significantly and positively related with NDVI across mainland Australia, with a typical time scale of soil moisture preceding NDVI by one month. Yang et al. (2014) demonstrate total water storage anomaly (TWSA) derived from the Gravity Recovery and Climate Experiment (GRACE) is a better sign of surface greenness over mainland Australia relative to precipitation, and they argued spaceborne soil moisture was measured within top several centimeters, rather than root-zone moisture. Nevertheless, Mulga has a dimorphic root distribution with the majority of the root biomass in the top 10 cm of the soil (Cleverly et al., 2016b) and is highly susceptible to minor variation in the upper moisture content (Eamus et al., 2013). Along with the follow-on GRACE mission launched in 2018 (Flechtner et al., 2018), it offers a chance to comprehensively evaluate interactions between vegetation dynamics and multiple hydro-meteorological drivers (soil moisture, precipitation, and TWSA) in future research.

4.3. Assessment with tower-based GPP

We found moderate correspondence between satellite-observed SIF, EVI and tower-based GPP monthly climatologies in non-wet years (Fig. 9c, d), consistent with findings of Madani et al. (2017), in which they suggested that the weaker relationship in central Australia reflect greater SIF uncertainty over sparsely vegetated region relative to mesic ecosystem. By contrast, remarkably enhanced correlations between GPP and SIF or EVI in both wet years of 2010–2011 and 2016–2017 (Fig. 9e-g), along with closer slopes ($k \cong 1$), suggests that satellite-based variables can provide very good estimate of productivity of dryland vegetation under wet conditions.

Considering a notable mismatch between footprints of flux tower measurement and satellite observation, we investigated these relationships at a range of spatial resolutions (Fig. 10). Due to being located in an extensive high-density Mulga woodland, the coefficient of determination at AU-ASM was constantly around 0.6, regardless of increasing footprints from 0.25 *km* to 45 *km*, and this was consistently larger than those at AU-TTE as a consequence of its more heterogeneous landscape (Cleverly et al., 2016c). At a coarse spatial resolution (~50 km), the relationship between GPP and EVI at AU-TTE was weaker than that for 5 km footprints, and the strength of correspondence of both sites was closer owing to overlapped footprints. Conversely, widely fluctuated relationships concerning SIF reveal that this product perhaps remains with much uncertainty and its high retrieval noise in low productivity region induces notable speckling relative to EVI and GPP (Gentine and Alemohammad, 2018; Geruo et al., 2017). On a basis of spatially coarse resolution and degradation of GOME-2 instrument, heterogeneity remains in the biome-level analysis though we set stringent criteria for “pure” pixels selection. In addition, the scarcity of flux tower sites in the interior of Australia impedes broad validation of satellite observations over most vegetation types.

4.4. Limitations and future work

Re-emitted chlorophyll fluorescence, in vivo to reflect photosynthetic dynamics in real time, is theoretically assumed to be a more rapid indicator relative to changes in canopy chlorophyll content as measured by reflectance-based vegetation index. Existing spaceborne SIF retrievals with multiyear records, such as GOME-2, the Greenhouse Gases Observing Satellite (GOSAT), and the SCanning Imaging Absorption spectroMeter for Atmospheric CHartographyY (SCIAMACHY), are generally provided with coarse spatial and temporal resolutions. There is a wide disparity in grid size between satellite-based SIF and EVI, and the monthly temporal resolution of satellite observations in this study may dampen the actual differences in the responses of SIF and EVI. Given that dryland vegetation is dynamic and responds within days to a precipitation pulse, we further examined the performance of EVI and SIF responses to both wet pulses at a finer temporal interval. Daily orbital SIF products (Level-2) were gridded and aggregated into 16-day records, consistent with MODIS EVI (MYD13C1). Relative to monthly SIF products (Level-3), the processed SIF time series with higher temporal resolution exhibited more erratic behavior with high variability, giving rise to more uncertainty and bias over water-limited ecosystems. Restricted by low signal levels and inherent noise, there is a trade-off in providing data quality and reliability of spaceborne SIF products and spatial/temporal resolution.

For a more in-depth study, improved SIF datasets with higher spatiotemporal resolution comparable with the footprint of flux tower measurement would be highly needed. Newly available physiologically-based proxy SIF from the TROPOspheric Monitoring Instrument (TROPOMI) with substantially enhanced spatial resolution has great potential for tracking and characterizing large-scale vegetation dynamics under changing climate (Doughty et al., 2019; Köhler et al., 2018; Leng et al., 2022). Among multiple surface reflectance-based proxies, Wang et al. (2022) found that SIF retrieved from TROPOMI and near-infrared reflectance index were the best performing GPP proxies and captured complementary aspects of seasonal GPP dynamics across dryland vegetation over the western United States. The Orbiting Carbon Observatory-2 (OCO-2) SIF product, with spatial resolution of approximately 1.3 × 2.25 km^2, offers promising opportunities for studying the SIF-GPP relationship and vegetation functional gradients at different spatiotemporal scales (Sun et al., 2017; Wang et al., 2020). These state-of-the-art spaceborne instruments along with upcoming missions will significantly contribute to revolutionizing our ability to accurately trace vegetation dynamics (Smith et al., 2019).

5. Conclusions

We have examined the response of satellite-observed SIF and EVI to the 2010–2011 big wet as well as a recent extreme wet pulse in 2016–2017 over arid central Australia, which is mainly covered by Hummock grasslands, Mulga woodlands, and Mulga shrublands. We found EVI was significantly responsive to both extreme wet events, with a markedly amplified seasonal amplitude. In contrast to predominantly positive anomalies of SIF in 2010–2011, SIF over nearly half of the region showed negative anomalies in 2016–2017 wet pulse. Although C4-dominated Hummock grasslands experienced larger amount of rainfall in 2016–2017, C3-dominated Mulga woodland was invariably the most responsive biome, attributed to its strong sensitivity to moisture availability. In spite of a robust linear SIF-GPP relationship at site level, SIF derived from GOME-2 has imperfect capacity for capturing spatial dynamics over xeric central Australia. This research provides a case study to reveal the process regarding interactions between climate anomalies and vegetation anomalies, which could be beneficial to other precipitation-driven ecosystems. With a projection of increasing extreme events in the future, identifying ecological responses to climate disturbances contributes to our understandings for sustainable managing of ecosystem services.

CRediT authorship contribution statement

Song Leng and Alfredo Huete conceived of the presented idea. Song Leng developed the theory and performed the computations. Alfredo Huete and Jamie Cleverly verified the analytical methods. Alfredo Huete and Qiang Yu supervised the findings of this work. All authors discussed the results and contributed to the final manuscript.

Declaration of competing interest

The authors declare that they have no known competing financial interests or personal relationships that could have appeared to influence the work reported in this paper.

Acknowledgement

The first author acknowledges the financial support from the joint CSC-UTS Scholarship between China Scholarship Council and University of Technology Sydney, Australia. We are thankful for the availability of flux tower data for public access by the Australian Terrestrial Ecosystem Research Network (TERN, www.tern.org.au) – OzFlux facility (www.ozflux.org.au).

Appendix A. Supplementary data

Supplementary data to this article can be found online at https://doi.org/10.1016/j.scitotenv.2022.156860.

References

Ahlström, A., Raupach, M.R., Schurgers, G., Smith, B., Arneth, A., Jung, M., Reichstein, M., Canadell, J.G., Friedlingstein, P., Jain, A.K., 2015. The dominant role of semi-arid ecosystems in the trend and variability of the land CO2 sink. Science 348 (6237), 895–899.

Andrew, R.L., Guan, H., Batelaan, O., 2017. Large-scale vegetation responses to terrestrial moisture storage changes. Hydrol. Earth Syst. Sci. 21 (9), 4469–4478. https://doi.org/10.5194/hess-21-4469-2017.

Barron-Gafford, G.A., Scott, R.L., Jenerette, G.D., Hamerlynck, E.P., Huxman, T.E., 2012. Temperature and precipitation controls over leaf-and ecosystem-level CO2 flux along a woody plant encroachment gradient. Glob. Chang. Biol. 18 (4), 1389–1400.

Biederman, J.A., Scott, R.L., Bell, T.W., Bowling, D.R., Dore, S., Garatuza-Payan, J., Kolb, T.E., Krishnan, P., Krofcheck, D.J., Litvak, M.E., 2017. CO 2 exchange and evapotranspiration across dryland ecosystems of southwestern North America. Glob. Chang. Biol. 23 (10), 4204–4221.

Bowman, D., Boggs, G.S., Prior, L.D., 2008. Fire maintains an Acacia aneura shrubland—Triodia grassland mosaic in central Australia. J. Arid Environ. 72 (1), 34–47.

Broich, M., Tulbure, M.G., Verbesselt, J., Xin, Q., Wearne, J., 2018. Quantifying Australia's dryland vegetation response to flooding and drought at sub-continental scale. Remote Sens. Environ. 212, 60–78. https://doi.org/10.1016/j.rse.2018.04.032.

Chen, C., Eamus, D., Cleverly, J., Boulain, N., Cook, P., Zhang, L., Cheng, L., Yu, Q., 2014. Modelling vegetation water-use and groundwater recharge as affected by climate variability in an arid-zone Acacia savanna woodland. J. Hydrol. 519, 1084–1096. https://doi.org/10.1016/j.jhydrol.2014.08.032.

Chen, T., de Jeu, R.A.M., Liu, Y.Y., van der Werf, G.R., Dolman, A.J., 2014b. Using satellite based soil moisture to quantify the water driven variability in NDVI: a case study over mainland Australia. Remote Sens. Environ. 140, 330–338. https://doi.org/10.1016/j.rse.2013.08.022.

Cleverly, J., Boulain, N., Villalobos-Vega, R., Grant, N., Faux, R., Wood, C., Cook, P.G., Yu, Q., Leigh, A., Eamus, D., 2013. Dynamics of component carbon fluxes in a semi-aridAcaciawoodland, central Australia. J. Geophys. Res. Biogeosci. 118 (3), 1168–1185. https://doi.org/10.1002/jgrg.20101.

Cleverly, J., Chen, C., Boulain, N., Villalobos-Vega, R., Faux, R., Grant, N., Yu, Q., Eamus, D., 2013. Aerodynamic resistance and Penman-Monteith evapotranspiration over a seasonally two-layered canopy in semiarid Central Australia. J. Hydrometeorol. 14 (5), 1562–1570. https://doi.org/10.1175/jhm-d-13-080.1.

Cleverly, J., Eamus, D., Luo, Q., Restrepo Coupe, N., Kljun, N., Ma, X., Ewenz, C., Li, L., Yu, Q., Huete, A., 2016. The importance of interacting climate modes on Australia's contribution to global carbon cycle extremes. Sci. Rep. 6, 23113. https://doi.org/10.1038/srep23113.

Cleverly, J., Eamus, D., Restrepo Coupe, N., Chen, C., Maes, W., Li, L., Faux, R., Santini, N.S., Rumman, R., Yu, Q., Huete, A., 2016. Soil moisture controls on phenology and productivity in a semi-arid critical zone. Sci. Total Environ. 568, 1227–1237. https://doi.org/10.1016/j.scitotenv.2016.05.142.

Cleverly, J., Eamus, D., van Gorsel, E., Chen, C., Rumman, R., Luo, Q., Coupe, N.R., Li, L., Kljun, N., Faux, R., Yu, Q., Huete, A., 2016. Productivity and evapotranspiration of two contrasting semiarid ecosystems following the 2011 global carbon land sink anomaly. Agric. For. Meteorol. 220, 151–159. https://doi.org/10.1016/j.agrformet.2016.01.086.

Dabernig, M., Mayr, G.J., Messner, J.W., Zeileis, A., 2017. Spatial ensemble post-processing with standardized anomalies. Q. J. R. Meteorol. Soc. 143 (703), 909–916.

Detmers, R.G., Hasekamp, O., Aben, I., Houweling, S., van Leeuwen, T.T., Butz, A., Landgraf, J., Köhler, P., Guanter, L., Poulter, B., 2015. Anomalous carbon uptake in Australia as seen by GOSAT. Geophys. Res. Lett. 42 (19), 8177–8184. https://doi.org/10.1002/2015gl065161.

Dikty, S., Richter, A., Weber, M., Noël, S., Bovensmann, H., Wittrock, F., Burrows, J.P., 2011. GOME-2 on MetOp-A Support for Analysis of GOME-2 In-orbit Degradation And Impacts on Level 2 Data Products. Final Report, Version. 1, p. 14.

Doughty, R., Köhler, P., Frankenberg, C., Magney, T.S., Xiao, X., Qin, Y., Wu, X., Moore, B., 2019. TROPOMI reveals dry-season increase of solar-induced chlorophyll fluorescence in the Amazon forest. Proc. Natl. Acad. Sci. 116 (44), 22393–22398.

Eamus, D., Cleverly, J., Boulain, N., Grant, N., Faux, R., Villalobos-Vega, R., 2013. Carbon and water fluxes in an arid-zone Acacia savanna woodland: an analyses of seasonal patterns and responses to rainfall events. Agric. For. Meteorol. 182–183, 225–238. https://doi.org/10.1016/j.agrformet.2013.04.020.

Eamus, D., Huete, A., Cleverly, J., Nolan, R.H., Ma, X., Tarin, T., Santini, N.S., 2016. Mulga, a major tropical dry open forest of Australia: recent insights to carbon and water fluxes. Environ. Res. Lett. 11 (12), 125011.

Evans, J.P., Meng, X., McCabe, M.F., 2017. Land surface albedo and vegetation feedbacks enhanced the millennium drought in south-east Australia. Hydrol. Earth Syst. Sci. 21 (1), 409–422. https://doi.org/10.5194/hess-21-409-2017.

Flechtner, F., Dahle, C., Landerer, F., Webb, F., Watkins, M., Massmann, H., Bettadpur, S., 2018. GRACE follow-on: current mission status and next steps. EGU General Assembly Conference Abstracts. 20, p. 8990.

Frankenberg, C., Fisher, J.B., Worden, J., Badgley, G., Saatchi, S.S., Lee, J., Toon, G.C., Butz, A., Jung, M., Kuze, A., 2011. New global observations of the terrestrial carbon cycle from GOSAT: patterns of plant fluorescence with gross primary productivity. Geophys. Res. Lett. 38 (17).

Gentine, P., Alemohammad, S.H., 2018. Reconstructed solar-induced fluorescence: a machine learning vegetation product based on MODIS surface reflectance to reproduce GOME-2 solar-induced fluorescence. Geophys. Res. Lett. 45 (7), 3136–3146. https://doi.org/10.1002/2017GL076294.

Geruo, A., Velicogna, I., Kimball, J.S., Du, J., Kim, Y., Colliander, A., Njoku, E., 2017. Satellite-observed changes in vegetation sensitivities to surface soil moisture and total water storage variations since the 2011 Texas drought. Environ. Res. Lett. 12 (5), 54006.

Guan, K., Pan, M., Li, H., Wolf, A., Wu, J., Medvigy, D., Caylor, K.K., Sheffield, J., Wood, E.F., Malhi, Y., Liang, M., Kimball, J.S., Saleska, S.R., Berry, J., Joiner, J., Lyapustin, A.I., 2015. Photosynthetic seasonality of global tropical forests constrained by hydroclimate. Nat. Geosci. 8 (4), 284–289. https://doi.org/10.1038/ngeo2382.

Haverd, V., Smith, B., Trudinger, C., 2016. Process contributions of Australian ecosystems to interannual variations in the carbon cycle. Environ. Res. Lett. 11 (5). https://doi.org/10.1088/1748-9326/11/5/054013.

Huang, J., Yu, H., Guan, X., Wang, G., Guo, R., 2016. Accelerated dryland expansion under climate change. Nat. Clim. Chang. 6 (2), 166.

Huete, A.R., Restrepo-Coupe, N., Ratana, P., Didan, K., Saleska, S.R., Ichii, K., Panuthai, S., Gamo, M., 2008. Multiple site tower flux and remote sensing comparisons of tropical forest dynamics in Monsoon Asia. Agric. For. Meteorol. 148 (5), 748–760. https://doi.org/10.1016/j.agrformet.2008.01.012.

Jenkins, J.P., Richardson, A.D., Braswell, B.H., Ollinger, S.V., Hollinger, D.Y., Smith, M.-L., 2007. Refining light-use efficiency calculations for a deciduous forest canopy using simultaneous tower-based carbon flux and radiometric measurements. Agric. For. Meteorol. 143 (1–2), 64–79.

Joiner, J., Guanter, L., Lindstrot, R., Voigt, M., Vasilkov, A.P., Middleton, E.M., Huemmrich, K.F., Yoshida, Y., Frankenberg, C., 2013. Global monitoring of terrestrial chlorophyll fluorescence from moderate-spectral-resolution near-infrared satellite measurements: methodology, simulations, and application to GOME-2. Atmos. Meas. Tech. 6 (10), 2803–2823.

Joiner, J., Yoshida, Y., Vasilkov, A.P., Schaefer, K., Jung, M., Guanter, L., Zhang, Y., Garrity, S., Middleton, E.M., Huemmrich, K.F., Gu, L., Belelli Marchesini, L., 2014. The seasonal cycle of satellite chlorophyll fluorescence observations and its relationship to vegetation phenology and ecosystem atmosphere carbon exchange. Remote Sens. Environ. 152, 375–391. https://doi.org/10.1016/j.rse.2014.06.022.

Köhler, P., Guanter, L., Joiner, J., 2015. A linear method for the retrieval of sun-induced chlorophyll fluorescence from GOME-2 and SCIAMACHY data.

Köhler, P., Guanter, L., Kobayashi, H., Walther, S., Yang, W., 2018. Assessing the potential of sun-induced fluorescence and the canopy scattering coefficient to track large-scale vegetation dynamics in Amazon forests. Remote Sens. Environ. 204, 769–785. https://doi.org/10.1016/j.rse.2017.09.025.

Leng, S., Huete, A., Cleverly, J., Gao, S., Yu, Q., Meng, X., Qi, J., Zhang, R., Wang, Q., 2022. Assessing the impact of extreme droughts on dryland vegetation by multi-satellite solar-induced chlorophyll fluorescence. Remote Sens. 14 (7). https://doi.org/10.3390/rs14071581.

Ma, X., Huete, A., Yu, Q., Coupe, N.R., Davies, K., Broich, M., Ratana, P., Beringer, J., Hutley, L.B., Cleverly, J., 2013. Spatial patterns and temporal dynamics in savanna vegetation phenology across the North Australian Tropical Transect. Remote Sens. Environ. 139, 97–115.

Ma, X., Huete, A., Moran, S., Ponce-Campos, G., Eamus, D., 2015. Abrupt shifts in phenology and vegetation productivity under climate extremes. J. Geophys. Res. Biogeosci. 120 (10), 2036–2052. https://doi.org/10.1002/2015jg003144.

Ma, X., Huete, A., Cleverly, J., Eamus, D., Chevallier, F., Joiner, J., Poulter, B., Zhang, Y., Guanter, L., Meyer, W., Xie, Z., Ponce-Campos, G., 2016. Drought rapidly diminishes the large net CO2 uptake in 2011 over semi-arid Australia. Sci. Rep. 6, 37747. https://doi.org/10.1038/srep37747.

Madani, N., Kimball, J., Jones, L., Parazoo, N., Guan, K., 2017. Global analysis of bioclimatic controls on ecosystem productivity using satellite observations of solar-induced chlorophyll fluorescence. Remote Sens. 9 (6). https://doi.org/10.3390/rs9060530.

Min, S.-K., Zhang, X., Zwiers, F.W., Hegerl, G.C., 2011. Human contribution to more-intense precipitation extremes. Nature 470 (7334), 378.

Moore, C.E., Beringer, J., Donohue, R.J., Evans, B., Exbrayat, J.F., Hutley, L.B., Tapper, N.J., 2018. Seasonal, interannual and decadal drivers of tree and grass productivity in an Australian tropical savanna. Glob. Chang. Biol. 24 (6), 2530–2544. https://doi.org/10.1111/gcb.14072.

Nicolai-Shaw, N., Zscheischler, J., Hirschi, M., Gudmundsson, L., Seneviratne, S.I., 2017. A drought event composite analysis using satellite remote-sensing based soil moisture. Remote Sens. Environ. 203, 216–225. https://doi.org/10.1016/j.rse.2017.06.014.

Poulter, B., Frank, D., Ciais, P., Myneni, R.B., Andela, N., Bi, J., Broquet, G., Canadell, J.G., Chevallier, F., Liu, Y.Y., Running, S.W., Sitch, S., van der Werf, G.R., 2014. Contribution of semi-arid ecosystems to interannual variability of the global carbon cycle. Nature 509 (7502), 600–603. https://doi.org/10.1038/nature13376.

Qiu, B., Xue, Y., Fisher, J.B., Guo, W., Berry, J.A., Zhang, Y., 2018. Satellite chlorophyll fluorescence and soil moisture observations lead to advances in the predictive understanding of global terrestrial coupled carbon-water cycles. Glob. Biogeochem. Cycles 32 (3), 360–375. https://doi.org/10.1002/2017gb005744.

Rammig, A., Mahecha, M.D., 2015. Ecology: ecosystem responses to climate extremes. Nature 527 (7578), 315.

Ratzmann, G., Gangkofner, U., Tietjen, B., Fensholt, R., 2016. Dryland vegetation functional response to altered rainfall amounts and variability derived from satellite time series data. Remote Sens. 8 (12). https://doi.org/10.3390/rs8121026.

Reichstein, M., Falge, E., Baldocchi, D., Papale, D., Aubinet, M., Berbigier, P., Bernhofer, C., Buchmann, N., Gilmanov, T., Granier, A., 2005. On the separation of net ecosystem exchange into assimilation and ecosystem respiration: review and improved algorithm. Glob. Chang. Biol. 11 (9), 1424–1439.

Reynolds, J.F., Smith, D.M.S., Lambin, E.F., Turner, B.L., Mortimore, M., Batterbury, S.P.J., Downing, T.E., Dowlatabadi, H., Fernández, R.J., Herrick, J.E., 2007. Global desertification: building a science for dryland development. Science 316 (5826), 847–851.

Smith, W.K., Biederman, J.A., Scott, R.L., Moore, D.J.P., He, M., Kimball, J.S., Yan, D., Hudson, A., Barnes, M.L., MacBean, N., Fox, A.M., Litvak, M.E., 2018. Chlorophyll fluorescence better captures seasonal and interannual gross primary productivity dynamics across dryland ecosystems of southwestern North America. Geophys. Res. Lett. 45 (2), 748–757. https://doi.org/10.1002/2017gl075922.

Smith, W.K., Dannenberg, M.P., Yan, D., Herrmann, S., Barnes, M.L., Barron-Gafford, G.A., Biederman, J.A., Ferrenberg, S., Fox, A.M., Hudson, A., Knowles, J.F., MacBean, N., Moore, D.J.P., Nagler, P.L., Reed, S.C., Rutherford, W.A., Scott, R.L., Wang, X., Yang, J.,

2019. Remote sensing of dryland ecosystem structure and function: progress, challenges, and opportunities. Remote Sens. Environ. 233, 111401. https://doi.org/10.1016/j.rse.2019.111401.

Song, L., Guanter, L., Guan, K., You, L., Huete, A., Ju, W., Zhang, Y., 2018. Satellite sun-induced chlorophyll fluorescence detects early response of winter wheat to heat stress in the Indian Indo-Gangetic Plains. Glob. Chang. Biol. 24 (9), 4023–4037.

Sun, Y., Fu, R., Dickinson, R., Joiner, J., Frankenberg, C., Gu, L., Xia, Y., Fernando, N., 2015. Drought onset mechanisms revealed by satellite solar-induced chlorophyll fluorescence: insights from two contrasting extreme events. J. Geophys. Res. Biogeosci. 120 (11), 2427–2440. https://doi.org/10.1002/2015jg003150.

Sun, Y., Frankenberg, C., Wood, J.D., Schimel, D.S., Jung, M., Guanter, L., Drewry, D.T., Verma, M., Porcar-Castell, A., Griffis, T.J., 2017. OCO-2 advances photosynthesis observation from space via solar-induced chlorophyll fluorescence. Science 358 (6360).

Vicente-Serrano, S.M., Gouveia, C., Camarero, J.J., Beguería, S., Trigo, R., López-Moreno, J.I., Azorín-Molina, C., Pasho, E., Lorenzo-Lacruz, J., Revuelto, J., 2013. Response of vegetation to drought time-scales across global land biomes. Proc. Natl. Acad. Sci. 110 (1), 52–57.

Wang, C., Guan, K., Peng, B., Chen, M., Jiang, C., Zeng, Y., Wu, G., Wang, S., Wu, J., Yang, X., 2020. Satellite footprint data from OCO-2 and TROPOMI reveal significant spatio-temporal and inter-vegetation type variabilities of solar-induced fluorescence yield in the US Midwest. Remote Sens. Environ. 241, 111728.

Wang, X., Biederman, J.A., Knowles, J.F., Scott, R.L., Turner, A.J., Dannenberg, M.P., Köhler, P., Frankenberg, C., Litvak, M.E., Flerchinger, G.N., Law, B.E., Kwon, H., Reed, S.C., Parton, W.J., Barron-Gafford, G.A., Smith, W.K., 2022. Satellite solar-induced chlorophyll fluorescence and near-infrared reflectance capture complementary aspects of dryland vegetation productivity dynamics. Remote Sens. Environ. 270, 112858. https://doi.org/10.1016/j.rse.2021.112858.

Wutzler, T., Lucas-Moffat, A., Migliavacca, M., Knauer, J., Sickel, K., Šigut, L., Menzer, O., Reichstein, M., 2018. Basic and extensible post-processing of eddy covariance flux data with REddyProc. Biogeosciences 15 (16), 5015–5030.

Xie, Z., Huete, A., Restrepo-Coupe, N., Ma, X., Devadas, R., Caprarelli, G., 2016. Spatial partitioning and temporal evolution of Australia's total water storage under extreme hydroclimatic impacts. Remote Sens. Environ. 183, 43–52. https://doi.org/10.1016/j.rse.2016.05.017.

Yang, Y., Long, D., Guan, H., Scanlon, B.R., Simmons, C.T., Jiang, L., Xu, X., 2014. GRACE satellite observed hydrological controls on interannual and seasonal variability in surface greenness over mainland Australia. J. Geophys. Res. Biogeosci. 119 (12), 2245–2260.

Yang, J., Tian, H., Pan, S., Chen, G., Zhang, B., Dangal, S., 2018. Amazon drought and forest response: largely reduced forest photosynthesis but slightly increased canopy greenness during the extreme drought of 2015/2016. Glob. Chang. Biol. 24 (5), 1919–1934. https://doi.org/10.1111/gcb.14056.

Yoshida, Y., Joiner, J., Tucker, C., Berry, J., Lee, J.E., Walker, G., Reichle, R., Koster, R., Lyapustin, A., Wang, Y., 2015. The 2010 Russian drought impact on satellite measurements of solar-induced chlorophyll fluorescence: insights from modeling and comparisons with parameters derived from satellite reflectances. Remote Sens. Environ. 166, 163–177. https://doi.org/10.1016/j.rse.2015.06.008.

Zhang, Y., Joiner, J., Gentine, P., Zhou, S., 2018. Reduced solar-induced chlorophyll fluorescence from GOME-2 during Amazon drought caused by dataset artifacts. Glob. Chang. Biol. 24 (6), 2229–2230.